An Unexpected Decline in Spring Atmospheric Humidity in the Interior Southwestern United States and Implications for Forest Fires

TESS W. P. JACOBSON,[a,b] RICHARD SEAGER,[a] A. PARK WILLIAMS,[c] ISLA R. SIMPSON,[d] KAREN A. MCKINNON,[e,f,g] AND HAIBO LIU[a]

[a] *Lamont-Doherty Earth Observatory, Columbia University, Palisades, New York*
[b] *Department of Earth and Environmental Sciences, Columbia University, New York, New York*
[c] *Department of Geography, University of California, Los Angeles, Los Angeles, California*
[d] *Climate and Global Dynamics Laboratory, National Center for Atmospheric Research, Boulder, Colorado*
[e] *Department of Statistics and Data Science, University of California, Los Angeles, Los Angeles, California*
[f] *Institute of the Environment and Sustainability, University of California, Los Angeles, Los Angeles, California*
[g] *Department of Atmospheric and Oceanic Sciences, University of California, Los Angeles, Los Angeles, California*

(Manuscript received 26 July 2023, in final form 30 November 2023, accepted 8 January 2024)

ABSTRACT: On seasonal time scales, vapor pressure deficit (VPD) is a known predictor of burned area in the southwestern United States ("the Southwest"). VPD increases with atmospheric warming due to the exponential relationship between temperature and saturation vapor pressure. Another control on VPD is specific humidity, such that increases in specific humidity can counteract temperature-driven increases in VPD. Unexpectedly, despite the increased capacity of a warmer atmosphere to hold water vapor, near-surface specific humidity decreased from 1970 to 2019 in much of the Southwest, particularly in spring, summer, and fall. Here, we identify declining near-surface humidity from 1970 to 2019 in the southwestern United States with both reanalysis and in situ station data. Focusing on the interior Southwest in the months preceding the summer forest fire season, we explain the decline in terms of changes in atmospheric circulation and moisture fluxes between the surface and the atmosphere. We find that an early spring decline in precipitation in the interior region induced a decline in soil moisture and evapotranspiration, drying the lower troposphere in summer. This prior season precipitation decline is in turn related to a trend toward a Northern Hemisphere stationary wave pattern. Finally, using fixed humidity scenarios and the observed exponential relationship between VPD and burned forest area, we estimate that with no increase in temperature at all, the humidity decline alone would still lead to nearly one-quarter of the observed VPD-induced increase in burned area over 1984–2019.

SIGNIFICANCE STATEMENT: Burned forest area has increased significantly in the southwestern United States in recent decades, driven in part by an increase in atmospheric aridity [vapor pressure deficit (VPD)]. Increases in VPD can be caused by a combination of increasing temperature and decreasing specific humidity. As the atmosphere warms with climate change, its capacity to hold moisture increases. Despite this, there is a decrease in near-surface air humidity in the interior southwestern United States over 1970–2019, which during the summer is likely caused by a decline in early spring precipitation leading to limited soil moisture and evaporation in spring and summer. We estimate that this declining humidity alone, without an increase in temperature, would cause about one-quarter of the VPD-induced increase in burned forest area in this region over 1984–2019.

KEYWORDS: Humidity; Atmosphere-land interaction; Hydrologic cycle; Stationary waves; Forest fires; Atmosphere

1. Introduction

Over the last half century, the southwestern United States (herein referred to as "the Southwest United States" or "the Southwest") experienced dramatic increases in forest fire activity. One crucial quantity for representing the influence of climate on fire activity in the western United States is vapor pressure deficit (VPD), a measure of atmospheric aridity that quantifies how far from saturated the atmosphere is at a given temperature and humidity, that is, the difference between the saturation vapor pressure of air at a certain temperature e_s and the actual vapor pressure e_a. VPD is a skillful predictor of forest fire activity in the western United States on interannual time scales, with more explanatory power for forest area burned in a given year than any other individual climate variable or drought index (Seager et al. 2015; Abatzoglou and Williams 2016; Williams et al. 2019; Jacobson et al. 2022; Williams et al. 2014b). VPD has been climbing significantly in the Southwest over recent decades, largely due to warming and thus increases in saturation vapor pressure e_s (Seager et al. 2015; Zhuang et al. 2021; Chiodi et al. 2021). However, changes in humidity also affect VPD. Williams et al. (2014a) noted the important contribution of a large negative specific humidity anomaly to the extremely high VPD anomaly that corresponded to the anomalous 2011 fire season in the Southwest. Whether the water vapor content of the atmosphere over the Southwest increases or decreases with warming will dampen or augment the temperature-driven increase in VPD and affect fire favorable climate conditions accordingly.

Corresponding author: Tess W. P. Jacobson, tessj@ldeo.columbia.edu

DOI: 10.1175/JHM-D-23-0121.1

© 2024 American Meteorological Society. This published article is licensed under the terms of the default AMS reuse license. For information regarding reuse of this content and general copyright information, consult the AMS Copyright Policy (www.ametsoc.org/PUBSReuseLicenses).

Brought to you by NOAA Central Library | Unauthenticated | Downloaded 08/28/24 07:28 PM UTC

According to the Clausius–Clapeyron relationship, as the atmosphere warms, the water vapor content of the atmosphere would increase at a rate of ~7% K^{-1} provided that relative humidity stays approximately constant and there are no limitations on water availability (Held and Soden 2006). This would slow but not cancel the effect of warming on VPD. Indeed, the water vapor content of the globally averaged atmosphere seems to approximately obey Clausius–Clapeyron scaling in models and observations (Dai 2006; Held and Soden 2006; O'Gorman and Muller 2010; Douville et al. 2022; Simpson et al. 2023). However, it is not well understood to what degree the warming-driven specific humidity increase at Clausius–Clapeyron scaling will hold over land surfaces, particularly over moisture-limited regions such as the southwestern United States. Deviations from Clausius–Clapeyron scaling could arise due to differential warming responses of land and oceans and limited ocean-to-land moisture transport (Byrne and O'Gorman 2015), plant physiological responses to warming (Swann et al. 2016), limited evaporable soil water, and changes in the partitioning of precipitation between evapotranspiration and runoff (Cook et al. 2014; Mankin et al. 2019; Williams et al. 2022). Changes in the atmospheric transport of water vapor from oceans to land surface through circulation changes could also play a role as a result of both external forcings and internal variability (Gimeno et al. 2020). Therefore, diagnosing atmospheric moisture content changes in the Southwest in response to warming is crucial to advance our understanding of hydroclimate change relevant to ecosystems.

Previous work has suggested that near-surface specific humidity may have decreased over recent decades in the Southwest, and that, in particular, specific humidity on the hottest summer days is decreasing (Brown and DeGaetano 2013; Williams et al. 2014a; McKinnon et al. 2021; Chiodi et al. 2021; Scheff and Burroughs 2023). Since the turn of the millennium, the Southwest has generally shifted into a warmer and drier state, and this increase in aridity coincided with an increase in forest area burned. Temperature increases in the Southwest are largely due to anthropogenic warming, while the decadal decline in precipitation is associated with a shift toward the cold phase of the Pacific decadal oscillation (Lehner et al. 2018; Seager and Hoerling 2014; Seager et al. 2022). The soil moisture decline associated with the precipitation and temperature shift has brought the Southwest into one of the most severe megadroughts in 1200 years (Williams et al. 2020, 2022). The observed exponential increases in burned area in the West and Southwest are linked to increased atmospheric aridity, which can be measured by VPD, and reduced summer fuel moisture, which is driven by these decadal variations and anthropogenic warming (Williams et al. 2019; Abatzoglou and Williams 2016; Westerling et al. 2006; Zhuang et al. 2021).

Within the Southwest, there are two subregions of clearly differing precipitation climatologies that exert control over the seasonality of forest fires: a coastal region and an interior region (Fig. 1). The coastal Southwest includes most of California and has a Mediterranean-type climate (Seager et al. 2019). That is, it receives maximum precipitation from winter storms and very little precipitation in the summer half year. The interior Southwest receives some precipitation from the winter storm track, but also experiences a summer precipitation maximum from the North American monsoon (Douglas et al. 1993; Adams and Comrie 1997; Seager et al. 2022). Forest fires in these two regions each become most active in the respective month that has both minimum precipitation and maximum VPD. In the coastal Southwest, VPD climbs to a peak in July, when precipitation is at a minimum. In contrast, in the interior, monsoon onset and maximum temperature typically occurs in July while maximum VPD, minimum precipitation, and maximum burned forest area occur in June. Burned area in these two regions during the month of maximum burning is affected differently by antecedent climate conditions. Near the coast, anomalously high July burned area correlates with high VPD and low precipitation in the preceding half year, with the highest lag correlation coefficients ($r \sim 0.5$) for VPD in late spring and summer, and it correlates with high temperatures (represented here by saturation vapor pressure) in the preceding spring and summer [Fig. 1; see Jacobson et al. (2022) for a detailed examination of the relationship between antecedent climate and burned forest area in the coastal region]. In the interior, the correlation between June burned area and high VPD/temperature is notably higher (and statistically significant) in the few months directly preceding and following the June ignitions. Low antecedent humidity (vapor pressure) appears to play a role in winter and late spring into summer ($r \sim 0.3$), and the correlation with low precipitation increases consistently going into summer. Clearly in each region, some combination of reduced precipitation, low humidity, high temperatures, and high VPD in the preceding months can influence subsequent burned area, although the relationship between burned area with individual climate drivers may not rise to levels of statistical significance for the entire period. Therefore, by examining changes in the seasonal evolution of these variables, we can better understand how the fire-favorable climate landscape has changed in the Southwest over recent decades.

In this study, we examine trends in fire-relevant climate quantities in the interior Southwest, with the particular goal of explaining an observed decline in vapor pressure during the months bridging spring into summer. We first describe recent trends in VPD and its temperature- and humidity-driven components in the entire Southwest in reanalysis data, validating the latter using in situ observations from weather station data (section 3). We then turn our focus to the interior Southwest and characterize the climatological seasonal cycle of surface and atmospheric moisture in the interior using an atmospheric moisture-budget approach as described in Seager et al. (2014) and Ting et al. (2018) (section 4). To explain the decline in lower-tropospheric vapor pressure, we examine trends in these surface and atmospheric moisture budget terms in section 5, and we further investigate the circulation drivers of a spring precipitation decline in the region that contributes significantly to the changing overall surface water balance. Finally, we estimate the contribution of the vapor pressure decline to the burned forest area increase in the interior Southwest in section 6. Our findings are summarized in section 7.

Here, a clarification is necessary regarding our expectations, motives, and conclusions in characterizing and diagnosing these moisture trends in the Southwest. Using the data available to us

Brought to you by NOAA Central Library | Unauthenticated | Downloaded 08/28/24 07:28 PM UTC

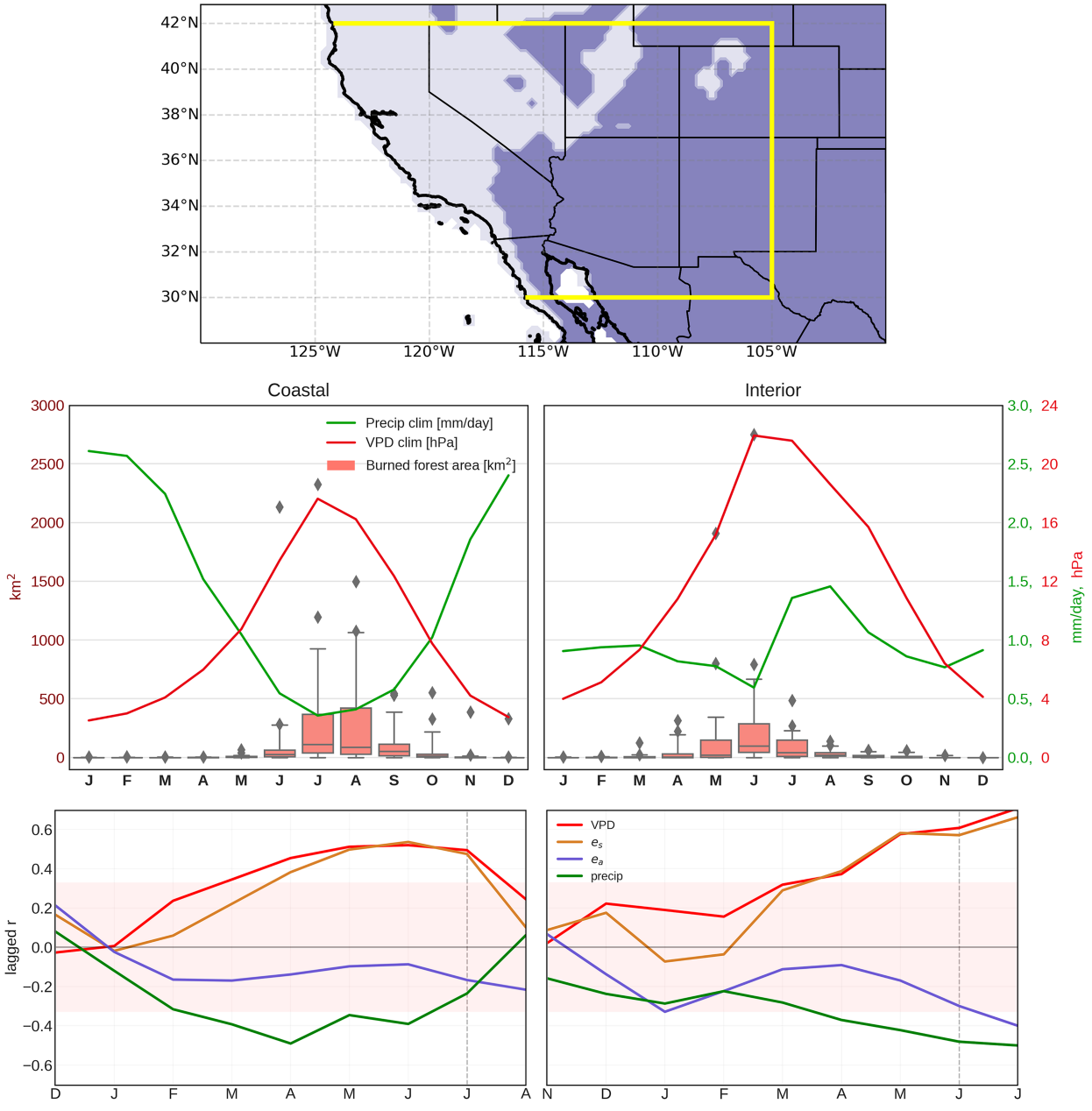


FIG. 1. (top) Coastal (light purple) vs interior (dark purple) precipitation regime regions in the Southwest. (middle) The respective monthly climatologies averaged over the coastal and interior regions, as defined by the light and dark purple regions within the yellow box in the top panel, of precipitation (green) and VPD (red) and burned forest area in boxplots with boxes indicating the interquartile range, whiskers at the 5th and 95th percentiles, and gray diamonds showing outliers. (bottom) Lagged correlation coefficients of the detrended natural logarithm of burned forest area [(left) July for the coastal region; (right) June for the interior] with detrended climate anomalies in the preceding seven months and following month. The red shaded region indicates the 95% significance threshold based on a two-sided Student's *t* test. The month of maximum fire activity is marked with a gray vertical dashed line.

from 1970 onward, namely, station observations and reanalyses, both of which have biases, we do not expect quantitative accuracy on the exact magnitude of the declines in atmospheric moisture, soil moisture, precipitation, or evaporation. It is not our intention to account for each gram of water in the atmosphere and land surface without robust observations extending back to the 1970s. Our goal in this work is rather to accurately report the *sign* of the vapor pressure trend, since our expectation from Clausius–Clapeyron is that e_a should increase with warming. Thus, a decrease in vapor pressure, substantiated by station observations, is notable for its *sign* alone. Similarly, we use the *signs* of the trends of other moisture-related quantities

Brought to you by NOAA Central Library | Unauthenticated | Downloaded 08/28/24 07:28 PM UTC

in the atmosphere and land surface to assign a plausible mechanism for the decline in vapor pressure. Consequently, we find it necessary to validate that the signs of these changes (in precipitation, soil moisture, and atmospheric humidity) are robust across multiple datasets in order to support the validity of the mechanism of drying that we argue for here. In the following, we find good agreement among these datasets on a long-term decline in spring precipitation, spring-to-summer soil moisture, and warm-season vapor pressure in the interior that lends confidence to this pathway of atmospheric drying.

2. Data and methodology

a. Burned area data

We use burned area data from the U.S. Forest Service's Monitoring Trends in Burn Severity (MTBS) product (Finco et al. 2012), which includes fires > 404 ha. The MTBS product from 1984 to 2019 is aggregated to monthly resolution such that burned area of each individual fire is attributed to the month of that fire's ignition, and we exclude prescribed burns. For forest fraction, we use the forest cover product from the National Land Cover Database (NLCD) (Homer et al. 2012), regridded to 1-km resolution. The NLCD includes eight land-cover products from 1992 to 2019. Forest fraction is approximated by assigning each 1-km grid cell with the maximum forest cover fraction of the eight NLCD products, as this represents a best estimate of prefire forest coverage. We then calculate burned forest area in a given region by multiplying forest cover fraction in each grid cell by the 1-km gridded MTBS burned area and aggregating over our chosen region.

b. Climate data

We use monthly means from fifth major global reanalysis produced by the European Centre for Medium-Range Weather Forecasts (ECMWF) (ERA5; Hersbach et al. 2020) for the 1970–2019 period, gridded at 0.25° resolution in longitude and latitude. We use ERA5 for precipitation, 2-m temperature, 2-m dewpoint, surface pressure, evaporation, runoff, soil moisture, winds, specific humidity, geopotential height, energy fluxes, and sea surface temperatures. For the transient terms in the moisture budget calculations, we use 6-hourly data from ERA5 for winds, surface pressure, and specific humidity. Anomalies of these quantities are calculated as deviations from the monthly climatologies over the 1970–2019 period. The 1970–2019 period is chosen for this analysis because ERA5 shows the most consistent agreement with station humidity data in the Southwest and with the atmospheric circulation in other reanalyses over this period.

To define the coastal and interior regions shown in Fig. 1, we use monthly precipitation climatologies from ERA5 over the 1970–2019 period. We define a climatological winter precipitation maximum as a local maximum during any month in November–April that is greater than the climatological precipitation in the two months preceding and following that month, and similarly for defining a summer precipitation maximum but using months May–October. The coastal region is defined as that with only winter precipitation maxima (a Mediterranean climate type), while the interior region is that with at least one precipitation maximum in summer (midlatitude semiarid and steppe climate types). We then smooth the mask with a 1° rolling window in longitude and latitude. For all analysis of the "interior" region in sections 3–5, we use the box 32°–37°N, 104°–114°W, which is almost entirely within the interior region as defined in Fig. 1.

VPD is calculated as the difference between saturation vapor pressure e_s and actual vapor pressure e_a, and e_s and e_a are calculated using 2-m temperature and dewpoint temperature following the methods of Seager et al. (2015). Lag correlations between VPD, e_s, and e_a and burned area are calculated using centered three-month rolling means of the monthly anomalies, after removing the 1970–2019 trend in both the climate variable and burned forest area time series.

We also compare precipitation and soil moisture data from ERA5 to several additional gridded products. For precipitation, we use the all-network precipitation product from the Parameter-Elevation Regressions on Independent Slopes Model (PRISM; Daly et al. 2008), precipitation from the Climatic Research Unit gridded Time Series (CRU TS; Harris et al. 2020), and the Multi-Source Weighted-Ensemble Precipitation (MSWEP) product (Awange et al. 2019). For soil moisture, we use top 1-m soil moisture from the Phase 2 North American Land Data Assimilation System (NLDAS-2) with the Noah land surface model (Xia et al. 2012) and root-zone soil moisture from the Global Land Evaporation Amsterdam Model (GLEAM), version 3.6a (Martens et al. 2017).

To assess the role of tropical Pacific SST variability in observed Northern Hemisphere circulation trends in section 5, we use the Mantua et al. (1997) Pacific decadal oscillation (PDO) index. The PDO contribution to March precipitation in the interior Southwest is calculated as the product of the regression coefficient of March precipitation onto the March PDO index, and the March PDO index itself. The PDO contribution to the March geopotential height trend is calculated using the regression coefficients and the trend in the PDO.

c. Station data

To validate humidity trends, we use daily 2-m dewpoint temperature from the Integrated Surface Database (ISD; Smith et al. 2011) Global Summary of the Day. From this we choose stations with data spanning 1970–2019 within the western United States (30°–50°N, 100°–125°W). For our analysis we choose to use only stations with relatively continuous data within this period; we define a "complete" season of data from a single station as a 3-month period (DJF, MAM, JJA, or SON) with more than 67 days of data, then choose only those stations with 150 or more "complete" seasons out of the 200 seasons in the 1970–2019 period (≥75% complete). We calculate vapor pressure from dewpoint temperature then aggregate the daily vapor pressure data to monthly means to calculate trends.

d. Moisture budget calculations

We calculate moisture budgets from ERA5 data as in Seager and Henderson (2013). In a steady-state atmosphere, the column-

Brought to you by NOAA Central Library | Unauthenticated | Downloaded 08/28/24 07:28 PM UTC

integrated moisture convergence can be represented as the difference between precipitation P and evaporation E:

$$P - E = -\frac{1}{g\rho_w}\nabla \cdot \int_0^{p_s} \mathbf{u} q dp, \tag{1}$$

where q is the specific humidity, $\mathbf{u}$ is the horizontal wind vector, p_s is the surface pressure, g is the gravitational constant, and ρ_w is the density of water. The column integrated moisture convergence [RHS of Eq. (1)] can also be separated into a monthly mean flow component and a submonthly transient eddy component, represented as

$$P - E = -\frac{1}{g\rho_w}\nabla \cdot \int_0^{p_s} \overline{\mathbf{u}}\,\overline{q} dp - \frac{1}{g\rho_w}\nabla \cdot \int_0^{p_s} \overline{\mathbf{u}'q'} dp, \tag{2}$$

where the overbar represents monthly means, and the prime represents departures from the monthly mean. Monthly and 6-hourly wind, humidity, and surface pressure data from ERA5 are used for these quantities, with the transient term calculated as the monthly mean of the 6-hourly $\mathbf{u}'q'$. We can further break down the mean flow term into three components representing the mean moisture advection, the mean mass convergence, and a surface boundary term, respectively, as follows:

$$-\nabla \cdot \int_0^{p_s} \overline{\mathbf{u}}\,\overline{q} dp = -\int_0^{p_s} \overline{\mathbf{u}} \cdot \nabla \overline{q} dp - \int_0^{p_s} (\nabla \cdot \overline{\mathbf{u}})\overline{q} dp - \overline{q_s \mathbf{u}_s} \cdot \nabla p_s. \tag{3}$$

For our purposes, the boundary term is calculated as a residual in (3) as recommended by Seager and Henderson (2013).

We also calculate horizontal moisture convergence by the mean flow at vertical levels over the interior southwest box using the divergence theorem, interpolating ERA5 q and $\overline{\mathbf{u}}$ to a standard 50-hPa resolution from 1000 to 250 hPa, and evaluating $\nabla \cdot q\overline{\mathbf{u}}$ over the surface as a closed line integral of $q\overline{\mathbf{u}}$ perpendicular to the border of the box at each level.

3. The observed decline in vapor pressure in the Southwest

We first characterize trends in VPD and its two constituent variables, saturation vapor pressure (e_s) and actual vapor pressure (e_a), in the entire Southwest over the 1970–2019 period. In every season, VPD increases extensively across the Southwest (Fig. 2). This increase is the largest and most widespread in JJA, when the VPD increase exceeds 6 mb (1 mb = 1 hPa) over 50 years in most of the western United States and northern Mexico, in both the coastal and interior regions. The spring (MAM) VPD increase is more concentrated in the interior Southwest, and in comparison, in autumn (SON), the VPD increase spreads westward into the coastal Southwest with maxima over California and the Sierra Nevada. The magnitude and spatial structure of the widespread warm-season VPD increase is largely driven by the increase in e_s. Since saturation vapor pressure increases exponentially with temperature, we would indeed expect atmospheric warming to drive this large increase in e_s that contributes to increasing VPD. This increased e_s is observed throughout the western United States in every season. However, we would also expect actual vapor pressure to rise in a warmer atmosphere, yet this is not the case for much of the Southwest, as evidenced in all seasons in Fig. 2. The decline in e_a (on the order of 1 mb over the 50-yr period) is most widespread in JJA but occurs also in MAM in the interior Southwest and in SON in both the coastal and interior Southwest. In these regions and seasons in particular, we observe a VPD increase that is *augmented* by the humidity decrease and is larger than would be expected from the temperature-driven increase in e_s alone.

Despite being sparse in space and time, data from weather stations in the Southwest corroborate the decline in vapor pressure. Figure 3 shows the monthly evolution and spatial distribution of the e_a trend in the Southwest from both ERA5 and stations. First, for the interior Southwest, here we can clearly see a decline in surface humidity that evolves, beginning in March, intensifying through June, and lingering through November. In the coastal region, there is drying throughout California and Nevada in February, concentrated in Southern California, from August through October. For simplicity in analyzing the interior drying trend using atmospheric moisture budgets, we define a box for the interior west (32°–37°N and 104°–114°W) that encloses much of the spring drying. In general, the magnitudes and signs of the trends in station data are well represented by ERA5.[1]

Figure 4 shows the e_a trends for each month at each station in the western United States (WUS, 30°–50°N, 100°–125°W) compared to the trend at the closest grid point in ERA5. In the entire WUS region, we find trends toward both increasing and decreasing e_a, with 75% agreement between ERA5 and ISD on the sign of the trend at a particular station and a particular month. In the interior box (scatters highlighted in yellow in Fig. 4), most stations and months have a negative e_a trend. When choosing only the trends in the interior Southwest in the months of March–June (scatters with red outline), we see that ERA5 and stations agree that e_a decreased *at every station in every month but one*. Thus, the decline in vapor pressure in the spring in the interior Southwest from 1970 to 2019 is a striking feature of both weather station data and reanalysis. Given the importance of this quantity to atmospheric drought and fire–climate interactions in this region, this drying tendency deserves a careful diagnosis. In the following sections, we focus on the drying trend in this interior, monsoonal region in the months bridging spring into summer, both because these are the months in which antecedent climate is most able to influence forest fire in its most active

[1] As shown in Simpson et al. (2023), the Japanese 55-year Reanalysis (JRA-55; Kobayashi et al. 2015) has a decline in surface specific humidity over 1980–2020, smaller than that in ERA5, while the Modern-Era Retrospective Analysis for Research and Applications, version 2 (MERRA-2; Gelaro et al. 2017), has essentially no change in this region, and notably does not assimilate station base humidity or near-surface satellite irradiances. While these reanalysis products disagree on the magnitude of the specific humidity decline in the Southwest, ERA5 agrees most closely with ISD measurements in the Southwest, making it valid to focus on ERA5 here (Simpson et al. 2023).

Brought to you by NOAA Central Library | Unauthenticated | Downloaded 08/28/24 07:28 PM UTC

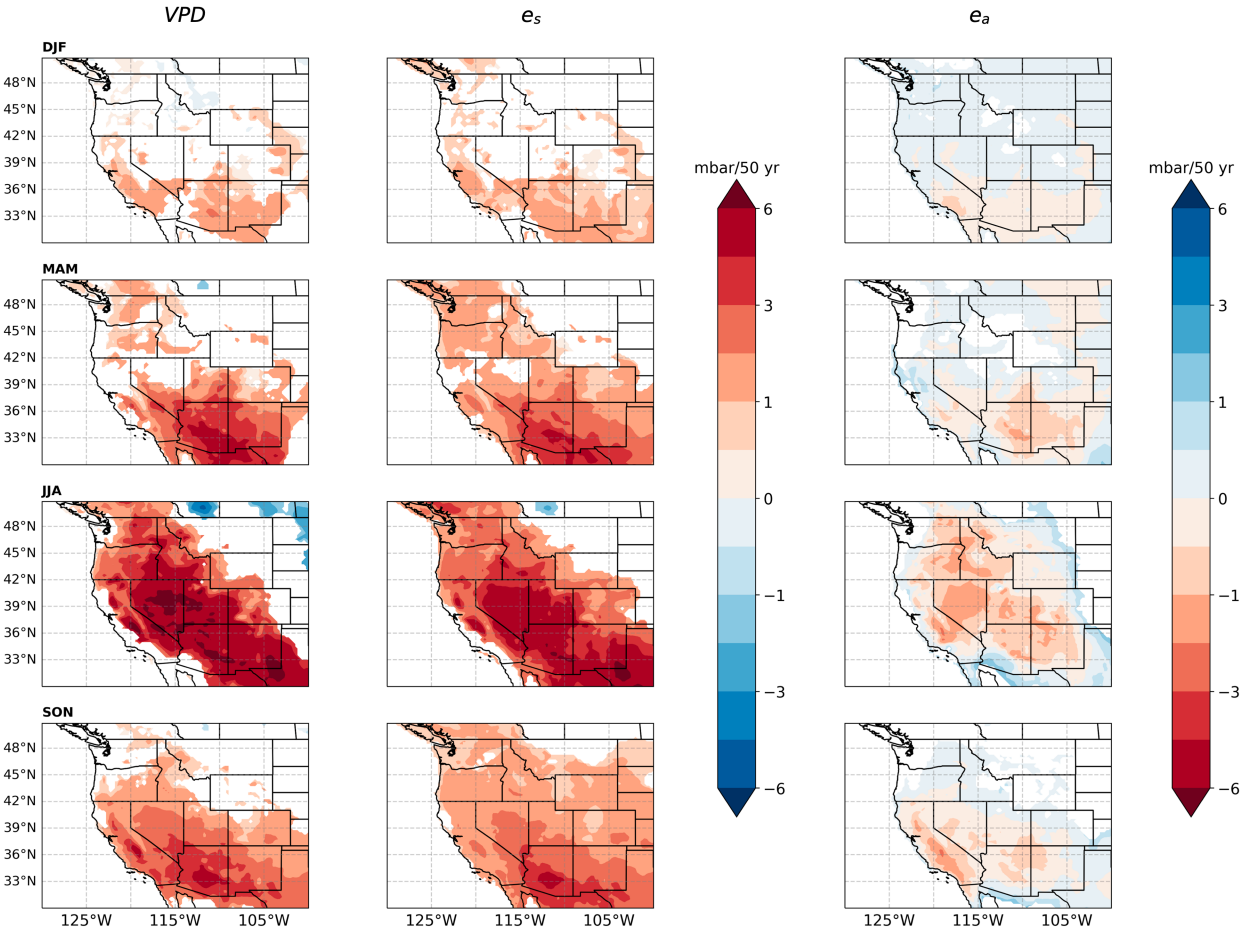


FIG. 2. Trends (as linear regression coefficients) by season in surface (left) VPD, (center) saturation vapor pressure (e_s), and (right) vapor pressure (e_a) in mb per 50 years over the 1970–2019 period from ERA5. VPD and e_s trends are shown only in regions where trends are significantly different from zero (p values are calculated from a two-sided Wald test, followed by correction for the false discovery rate of 0.1), while e_a trends are shown where the e_a trend is either negative or not significantly positive. Note the direction of the color bar on the right.

month (June) in the interior, and also because station data and reanalyses both show an intensification of near-surface drying in this region from March to June that is alleviated once the monsoon onsets in July. To explain the mechanisms behind this decline in e_a, we now turn to a characterization of the climatology and trends in the surface water and atmospheric moisture budgets of the interior Southwest, focusing on the months leading into the summer monsoon season.

4. Climatological seasonal cycle of surface and atmospheric moisture in the interior Southwest

To help understand the changes over time in the regional hydrology, we first consider the climatological state. The interior Southwest has a dual-peaked precipitation regime with a large precipitation peak during the North American monsoon (NAM) in July and August and a less pronounced winter rainy season centered about February (Fig. 5). Evaporation increases from a minimum in December to a monsoon-synced maximum in August. From October to March, which includes most of the winter rainy season, precipitation exceeds evaporation. However, top 1-m soil moisture declines from September to December (perhaps due to vertical moisture transport between soil levels and nonclosure of the surface water budget in assimilation) and only begins to increase again from December to March, lagged about three months from the beginning of the precipitation surplus. Going into summer from March to June, evaporation exceeds precipitation, and top 1-m soil moisture declines. During the monsoon (July and August), precipitation exceeds evaporation, and soil moisture increases lagged about a month from the July onset of the monsoon. Runoff in the region is small in comparison to P and E, and near zero for all months except for an increase from June into August as the monsoon ramps up, followed by a postmonsoon decrease.

The climatological atmospheric convergence of moisture aligns closely with this surface regime. During the NAM rainy season (July–September), the mean flow converges moisture into the region while transient eddies carry moisture out of

Brought to you by NOAA Central Library | Unauthenticated | Downloaded 08/28/24 07:28 PM UTC

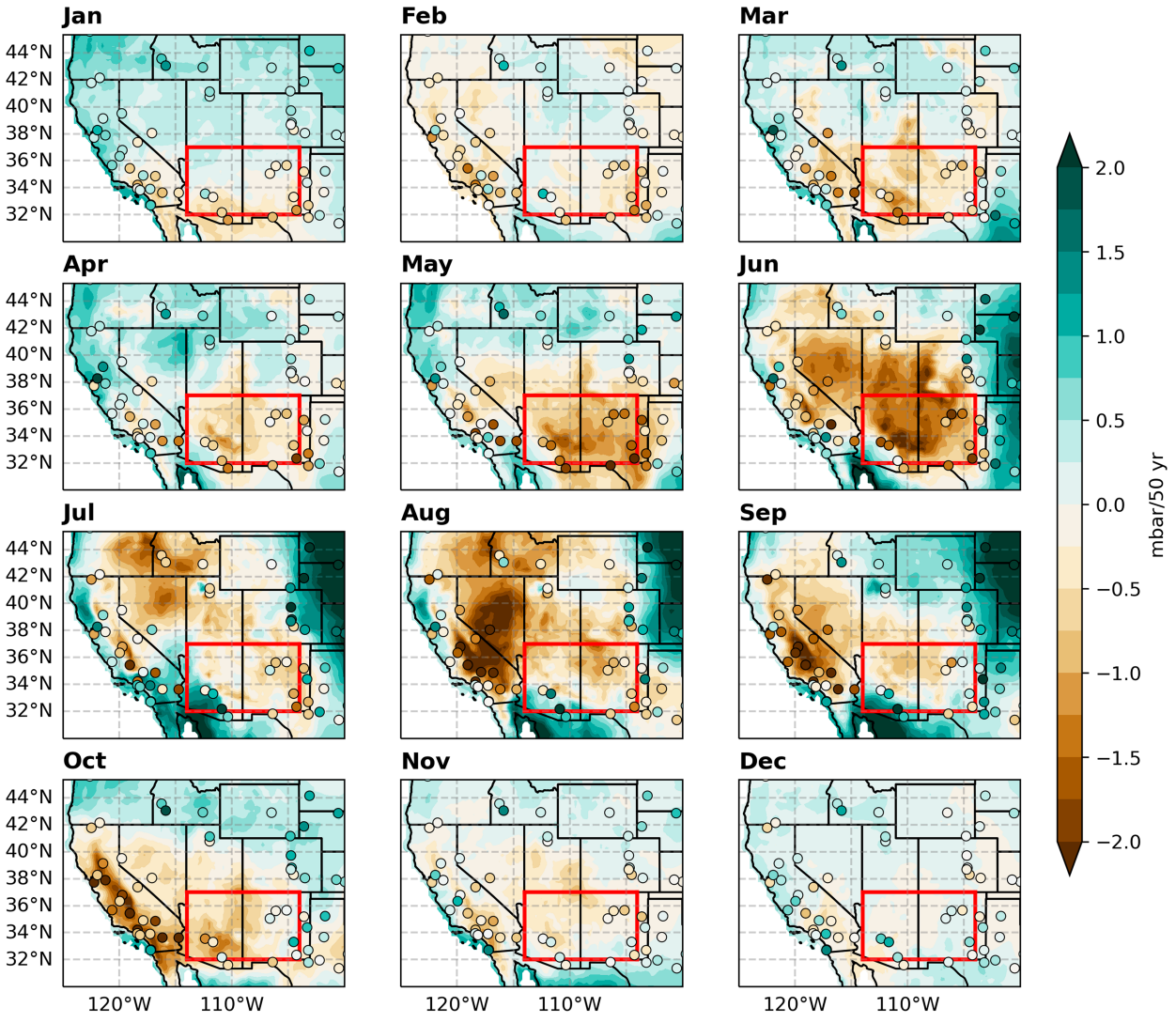


FIG. 3. Trends by month in vapor pressure (e_a) in mb per 50 years over the Southwest over the 1970–2019 period from ERA5 (colored shading) and ISD stations (colored scatter points). The box used for analysis of the interior Southwest is outlined in red, 32°–37°N and 104°–114°W.

the region (Fig. 5; note that our calculated moisture budget does not completely close and there is a small residual between $P - E$ and the sum of the mean flow and transient eddy terms.) The column moisture surplus peaks in July and is rained out as the monsoon begins. For the rest of the year, the mean flow and eddies have opposite contributions to the column moisture budget, with the mean flow diverging moisture from the column and the transient eddies converging moisture into the column. When split up into mass convergence by the mean flow, advection by the mean flow, and the residual surface term, we see that the large (~2 mm day^{-1}) convergence of moisture by the mean flow in July is predominantly due to orographic lift during the monsoon, as evidenced by the surface term in Fig. 5. This is consistent with recent understanding of the large contribution of orography and upslope winds to North American monsoon rainfall (Boos and Pascale 2021). The mean flow mass convergence is positive throughout the year with a peak in August, while the advection term is a divergence contribution for most of the year and strongest in the late spring to summer.

It is useful to see furthermore *where* in the column the mean flow is converging moisture throughout the year. To do so we calculated horizontal mean flow moisture convergence ($-\nabla \cdot \overline{q}\,\overline{\mathbf{u}}$) in 50-hPa layers of the atmosphere as a closed line integral around the region at each layer. In the top-right panel of Fig. 6, we see the low-level horizontal moisture convergence by the mean winds centered around the monsoon months. From February through October, there is some lower-level convergence of moisture by the mean winds underneath a moisture divergence. When the monsoon begins in July, this upper-level mean flow divergence almost stops entirely as the moisture is both rained out and diverged away by transient eddies (shown

Brought to you by NOAA Central Library | Unauthenticated | Downloaded 08/28/24 07:28 PM UTC

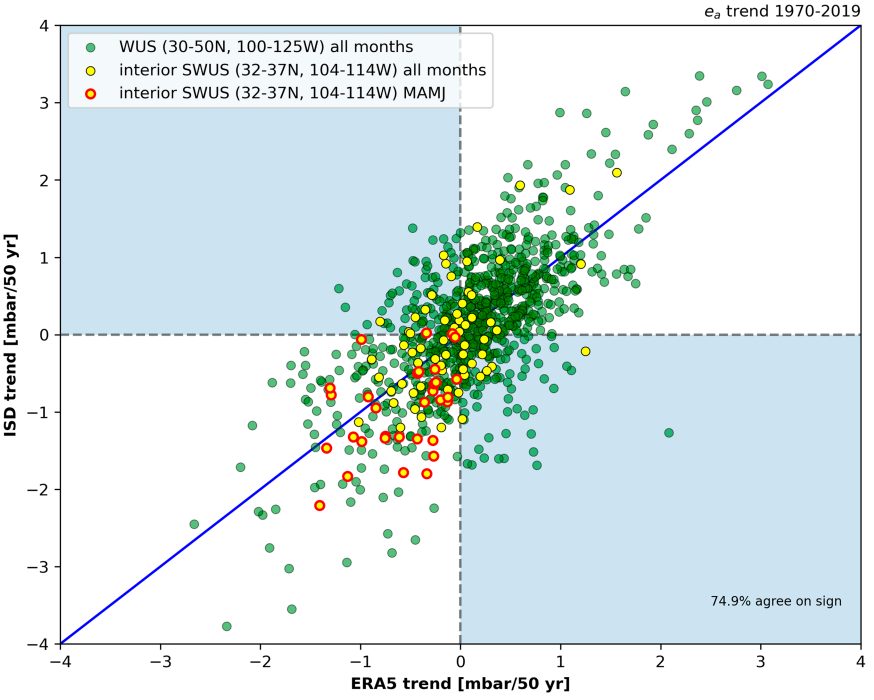


FIG. 4. Comparison of monthly e_a trends, in mb per 50 years, for each month and station in ISD to the trend in the nearest ERA5 grid point. Green scatters indicate trends from stations in the western United States (30°–50°N, 100°–125°W) in all months, yellow scatters indicate trends from stations within the interior Southwest box (32°–37°N, 104°–114°W) in all months, and yellow scatters with red outlines show trends from stations in the interior Southwest box specifically for the months of March, April, May, and June. The blue diagonal line indicates the 1:1 line.

in vertically integrated quantities in Fig. 5). There is ascent in the summer half year, centered around 750 hPa in June and strong subsidence throughout the troposphere in the wintertime. In terms of moisture transport by the horizontal winds, this region experiences weak surface westerlies and stronger flow aloft, with a break in the westerlies in July and August during the monsoon. There is southerly flow for most of the year at the surface and extending up to about 600 hPa in summer, and there are northerlies above 700 hPa from November to March. The picture emerges of moist lower-tropospheric westerly inflow in winter transitioning into strong surface–midtroposphere southerly inflow in the summer monsoon season accompanied by lower-tropospheric ascent.

5. Seasonal evolution of trends in surface and atmospheric moisture

Over the 1970–2019 period, the interior Southwest experienced declines in precipitation, evaporation, runoff (not shown), and soil moisture in the months leading into the monsoon season (Fig. 7). The precipitation trend in January and February was small (<0.1 mm day^{-1} over 50 years), but there was a sharp decline in March (over 0.7 mm day^{-1} over 50 years, compared to an average March precipitation of 0.95 mm day^{-1} and thus a 77% decline). This might correspond to a more rapid shutdown of the winter rainy season in early spring. Negative precipitation trends continue through spring and summer. June, the month with the least climatological precipitation in this region, experienced a 56% decline in precipitation. Evaporation trends by month are consistent with these precipitation changes. In particular, from spring into summer, changes in evaporation seem to be in response to the dramatic March decline in precipitation. The seasonal evolution of the evaporation trends is more monotonic from winter to summer than the precipitation trends, and the evaporation decline is larger than the corresponding decline in precipitation from April to August. Both surface (0–7 cm) and top 1-m soil moisture decline in every month, with the strongest decline found in April following the sharp March precipitation reduction. This implies that a prior-season precipitation decline is limiting evaporable water in the soil, reducing evaporation in the months following March. The March–June soil moisture decline is well reproduced in other land surface and soil moisture models as shown in Fig. 8, although the magnitude of the decline is largest and possibly overestimated in ERA5 given the closer agreement on the magnitude of the trend and variability between the other two land surface models (NLDAS-Noah and GLEAM). This is consistent, too, with a larger March precipitation decrease in ERA5 compared to other observation-based precipitation products (see Fig. 10).

Above the surface, large changes in the column-integrated moisture convergence from the mean flow and transient eddies can further inform about the atmospheric mechanisms involved

Brought to you by NOAA Central Library | Unauthenticated | Downloaded 08/28/24 07:28 PM UTC

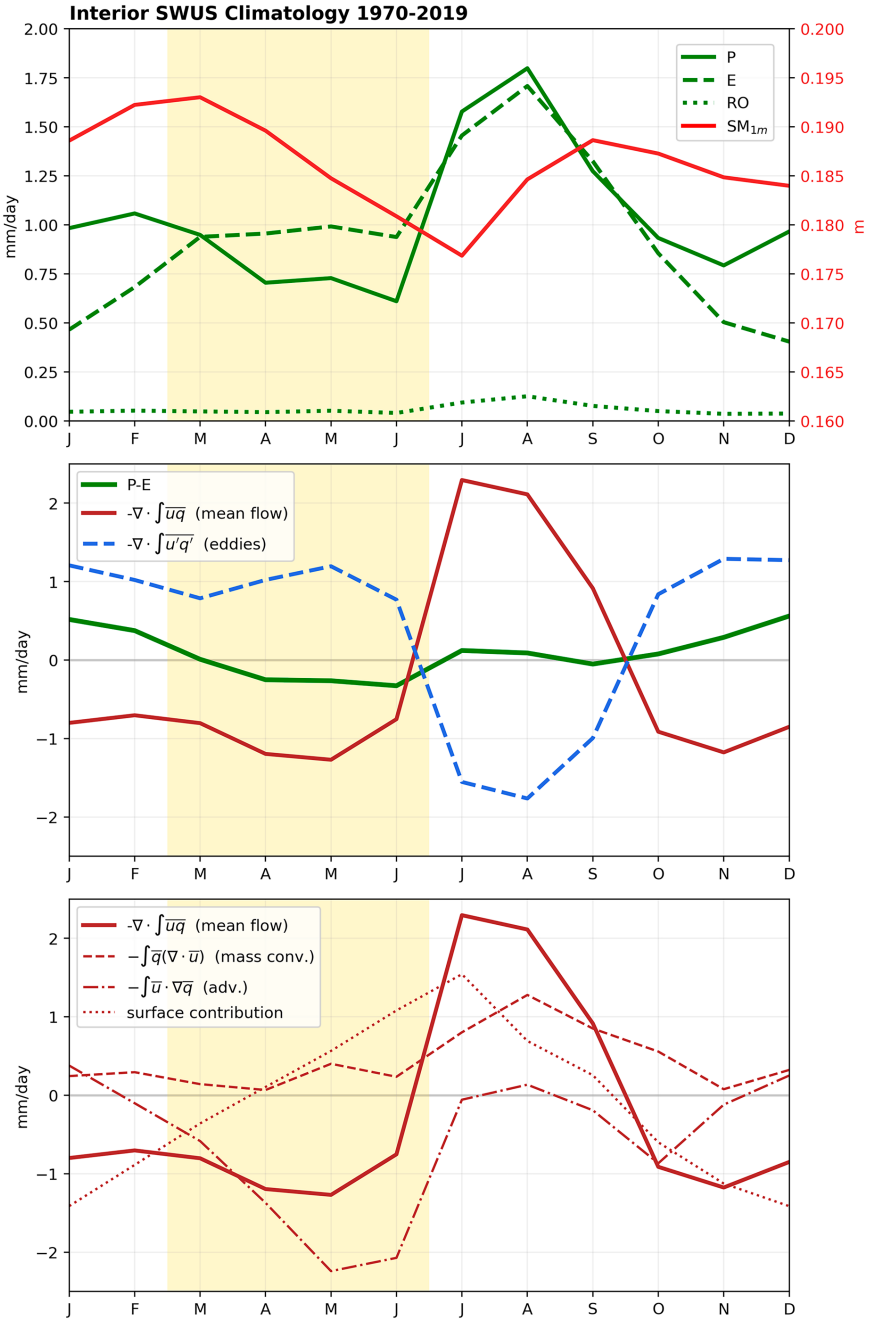


FIG. 5. (top) Monthly climatologies of surface water balance variables (precipitation, evaporation, runoff, and top meter soil moisture); (middle) column-integrated atmospheric moisture budget terms (precipitation minus evaporation, moisture convergence by the mean flow, and moisture convergence by transient eddies); and (bottom) breakdown of the mean flow moisture convergence (mean flow moisture convergence, mass convergence by the mean flow, moisture advection by the mean flow, and a surface term) in the 32°–37°N, 104°–114°W region over the 1970–2019 period. All units are mm day^{-1} except for soil moisture, which is given in meters with the soil moisture axis in red on the right-hand side of the leftmost panel. The months of March–June are shaded in yellow.

Brought to you by NOAA Central Library | Unauthenticated | Downloaded 08/28/24 07:28 PM UTC

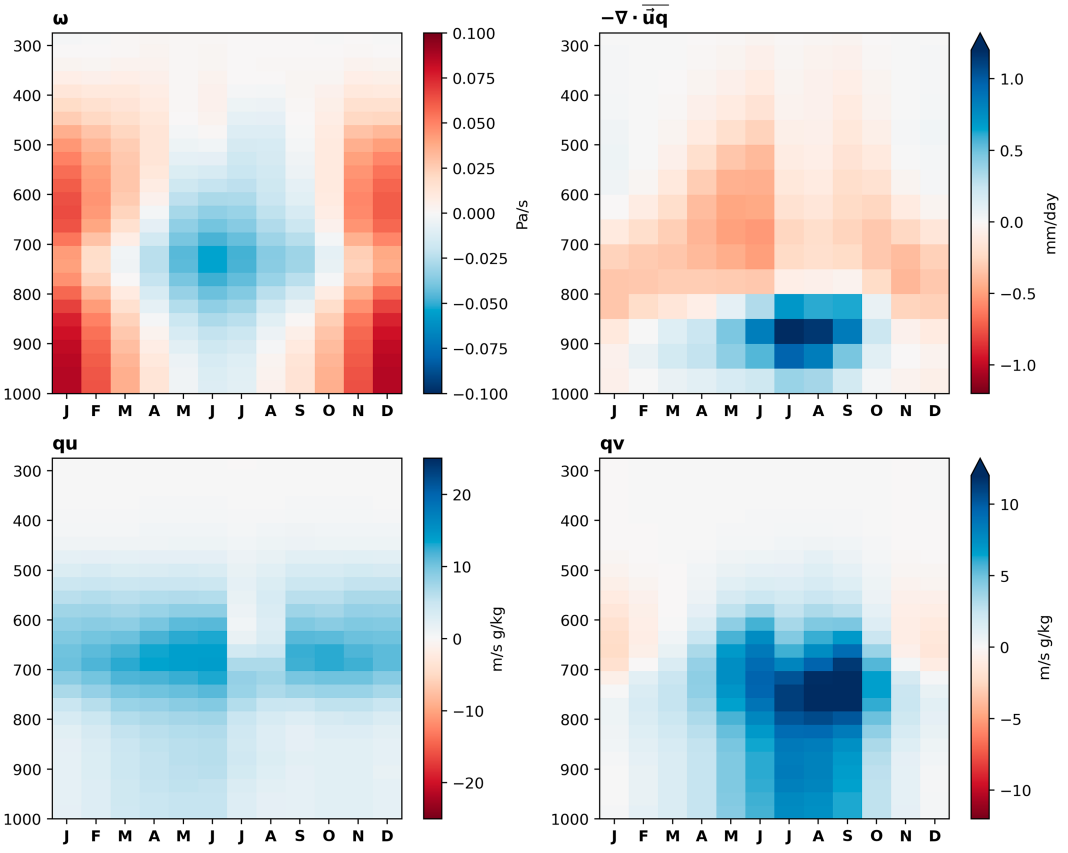


FIG. 6. (top left) Monthly climatology of subsidence (ω), (top right) horizontal moisture convergence by the mean flow ($-\nabla \cdot \overline{q}\,\overline{\mathbf{u}}$), (bottom left) zonal moisture transport (qu), and (bottom right) meridional moisture transport (qv) at pressure levels from 1000 to 250 hPa, in the 32°–37°N, 104°–114°W region over the 1970–2019 period.

in the lower-tropospheric humidity decline. In January and February, when transient eddies are typically converging moisture into the column and the mean flow is diverging moisture out of the column (Fig. 5), both of these terms are weakening compared to their climatological contributions to the moisture budget (Fig. 7). That is, the trend is such that transient eddies converge *less* moisture and the mean flow diverges *less* moisture, though the mean flow change is larger. The sharp decline in March precipitation appears to be a result of strengthening climatological moisture divergence by the mean flow. In April through June (AMJ), when climatological $P - E$ is negative, both the mean flow and the transient eddies are converging

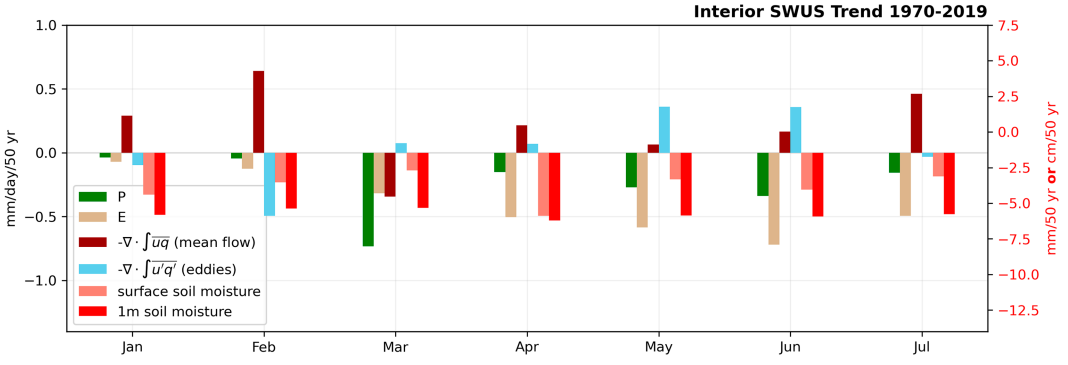


FIG. 7. Trends by month from January to July over the 1970–2019 period in precipitation, evaporation, moisture convergence by the mean flow, moisture convergence by transient eddies, surface (0–7 cm) soil moisture, and top 1-m soil moisture. Units are mm day^{-1} per 50 years except for soil moisture, which is in mm per 50 years for surface soil moisture and cm per 50 years for top meter soil moisture, with the axis in red on the right-hand side.

Brought to you by NOAA Central Library | Unauthenticated | Downloaded 08/28/24 07:28 PM UTC

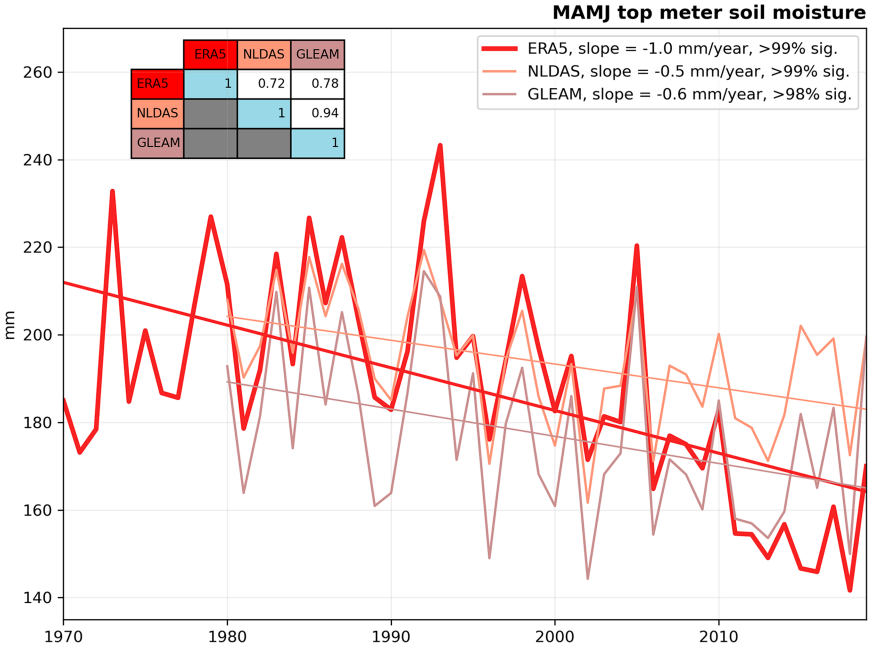


FIG. 8. Top meter soil moisture in the interior Southwest averaged over the months of March–June from 1970 to 2019 in ERA5 (red) compared to the same quantity from NLDAS-Noah from 1980 to 2019 (orange) and root-zone soil moisture from GLEAM from 1980 to 2019 (brown). The linear trend lines over the respective periods are plotted as well, with the slopes and significance of the trends noted in the legend, where significance is calculated as the p values from a two-sided Wald test. The table in the upper-left corner shows Pearson correlation coefficients between the datasets over the 1980–2019 period.

more moisture into the column, associated with a trend toward increased $P - E$ during this period. This is because the precipitation declines less than evaporation. The large negative trend in evaporation in AMJ represents a decreased flux of moisture from the surface to the lower atmosphere and is therefore a likely source of the decreased surface e_a. This is bolstered by a close spatial match more broadly between the western U.S. regions where evaporation and soil moisture are decreasing and the regions where e_a is decreasing (not shown). This is consistent with the increased column moisture convergence: with a drier lower atmosphere, where the majority of moisture transport occurs, the mean flow moisture divergence will decrease and since horizontal moisture gradients are strengthened, transient eddy moisture convergence will increase. Spatial analysis of moisture flux trends in the Southwest suggest that the transient eddies act diffusively to decrease moisture gradients over this period (not shown), which is in accordance with our understanding from similar analyses of the role of transient eddy moisture convergence in diffusing moisture gradients, including those induced by climate change, over North America (Seager et al. 2014).

We see some evidence of this process occurring in the atmospheric column in Fig. 9. The trends in mean flow horizontal moisture convergence ($-\nabla \cdot \overline{q}\overline{\mathbf{u}}$) and subsidence reflect the mechanism described above. In March, when the precipitation decline is at a maximum, the mean flow diverges moisture in the lower troposphere and there is increased subsidence in the midtroposphere, linked to suppressed precipitation at the end of the winter season. Then, from April through June, the lower-tropospheric mean flow moisture convergence tendency is positive (though weak) as the atmosphere responds to the lower-tropospheric drying by converging more moisture. In terms of horizontal moisture transport, the large decline in March precipitation is accompanied by large declines in the eastward and, to a lesser extent, northward transports of moisture in March.

Thus, the mechanism behind the decrease in spring e_a seems to be as follows: a long-term decline in early spring precipitation in this region leads to a similar long-term decline in evaporable soil water. This causes a decline in evaporation in spring that exceeds the decline in precipitation on monthly scales. In response to the decline in evaporation, the lower troposphere dries out. In response to this drying, the atmosphere converges more moisture into the lower troposphere to partially offset the surface-driven drying, but the column remains anomalously dry and the decline in precipitation is maintained through late spring and summer. Crucially, this mechanism differs from one in which atmospheric humidity declines due to concomitant circulation changes that cause anomalous dry advection into the region, or anomalous subsidence, moisture divergence, and potentially enhanced evapotranspiration throughout the whole spring. What we describe is rather drying where the mechanisms are seasonally dependent, with an important role for surface forcing in late spring and summer, after a change in circulation causes a long-term change in the surface water balance in early

Brought to you by NOAA Central Library | Unauthenticated | Downloaded 08/28/24 07:28 PM UTC

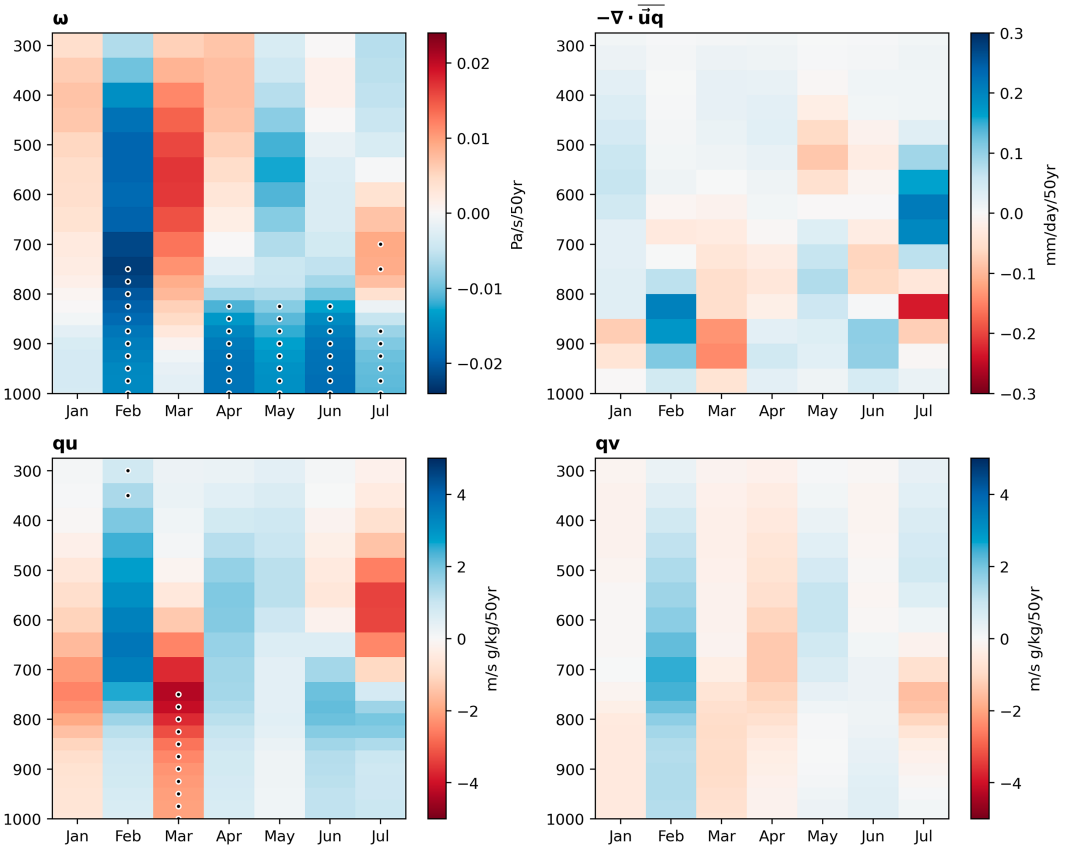


FIG. 9. As in Fig. 6, but showing trends over the 1970–2019 period in the months of January–July. Dots show months and levels where trends are significantly different from zero (p values are calculated from a two-sided Wald test, followed by correction for a false discovery rate of 0.2).

spring. This soil moisture–evapotranspiration-driven drying is similar to the mechanism identified in McKinnon et al. (2021) during hot, dry summers in the broader Southwest.

We now turn to look for circulation drivers of the March precipitation decline. The time series of March precipitation in the interior Southwest is shown for ERA5 and several gridded observational products on the right in Fig. 10. There is good agreement on the interannual variability and trend of March precipitation over this period between multiple datasets, though the ERA5 March precipitation decline is slightly larger in magnitude than in CRU and PRISM (~−0.7 versus ~−0.6 mm day^{-1} per 50 years). This could be related to the larger decline in spring-to-summer soil moisture in ERA5 compared to other land surface datasets (Fig. 8).

The reduction in March precipitation is concurrent with a trend toward an extratropical Rossby wave, dominated by

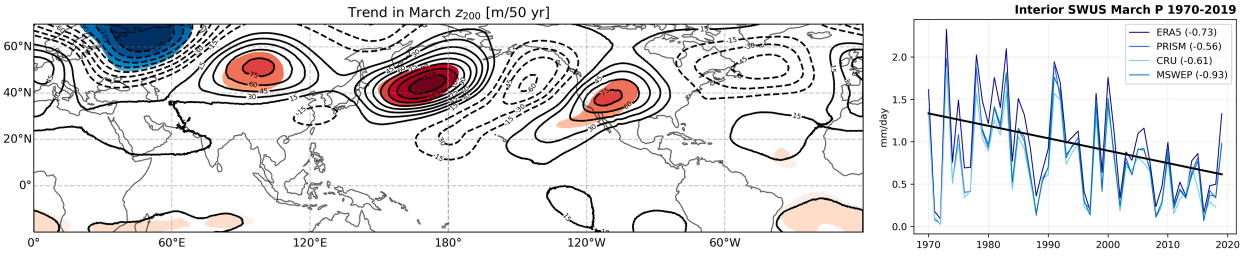


FIG. 10. Trend over 1970–2019 in March geopotential height at 200 hPa (z_{200}) in meters per 50 years, with the global mean removed, colors shown where trends over 50 years are larger than one standard deviation of the interannual variability. On the right, March precipitation time series over the 1970–2019 period from ERA5, PRISM, CRU, and MSWEP, with the linear trendline for ERA5 precipitation shown in black. The slopes of the March precipitation trends from each dataset are in parentheses in the legend, in units of mm day^{-1} per 50 years (note that MSWEP begins in 1979 while the other products are available at least starting in 1970).

Brought to you by NOAA Central Library | Unauthenticated | Downloaded 08/28/24 07:28 PM UTC

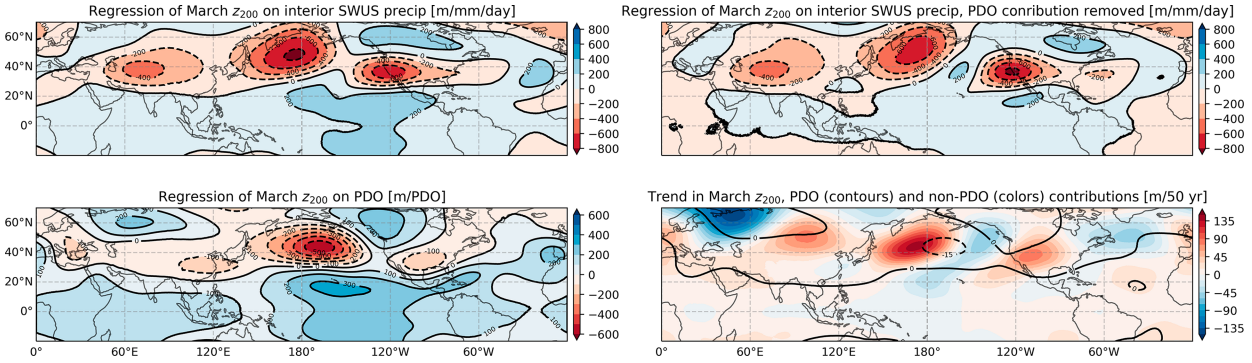


FIG. 11. (top left) Regression coefficients of March z_{200} regressed onto anomalous March precipitation in the interior Southwest (m mm^{-1} day^{-1}). (top right) Regression coefficients of March z_{200} regressed onto anomalous non-PDO related March precipitation in the interior Southwest (m mm^{-1} day^{-1}). (bottom left) Regression coefficients of March z_{200} regressed onto the PDO index (m per PDO index). (bottom right) PDO contribution to the trend in March z_{200} (contours) and residual non-PDO-related trend in March z_{200} (colors) with the area-weighted global mean removed (m per 50 years). Contour intervals are 15 m per 50 years, and red indicates a positive trend.

wavenumber 4, in the Northern Hemisphere that places a high pressure over the western United States as shown by the trend in 200-hPa geopotential height in Fig. 10. The wave trend is relatively barotropic, thus impacting low-level flow too (not shown). The interior Southwest lies along the southern flank of the center of the western U.S. high pressure trend, and the associated increased easterly flow over the mountain ranges of western North America will tend to suppress precipitation on the leeward side of the mountains. Ultimately it is the trend toward this high pressure, as part of an extratropical wave, increased subsidence, decreased zonal moisture transport, and decreased mean flow moisture convergence that drives the decrease in March precipitation.

Previous work has suggested a role for decadal-scale SST variability in the tropical Pacific, namely, the PDO, in influencing wintertime precipitation trends in the Southwest via atmospheric teleconnections (Lehner et al. 2018). By regressing March geopotential height onto March precipitation in the interior Southwest, we see that reduced precipitation in the interior Southwest is associated with a wavelike pattern in the midlatitudes along with twin low pressure anomalies in the equatorial Pacific (Fig. 11, top left). The midlatitude wave pattern and the twin low pressures are significantly different from zero using p values calculated from a two-sided Wald test followed by correction for a false discovery rate of 0.2 (not shown). This indicates that precipitation in the region is likely influenced by both tropical SST variability and other interannual atmospheric variability in the midlatitudes. We can further examine the relevance of the PDO to this height signal by decomposing the precipitation time series in the interior Southwest into a component linearly dependent on the PDO and a residual component linearly independent of the PDO. When we regress z_{200} onto the interior Southwest precipitation that is linearly independent of the PDO, the tropical (PDO-related) signal disappears and the wavelike pattern to the north more closely resembles the trend in Fig. 10 (Fig. 11, top right). The height pattern associated with the PDO itself is shown in the bottom left of Fig. 11, where we see that the negative phase of the PDO is associated with twin low pressure anomalies in the equatorial Pacific and midlatitude high pressure anomalies east of the date line and over the United States, and thus drier conditions in the Southwest. Similarly, we can decompose the z_{200} trend itself into its PDO- and non-PDO-related contributions (Fig. 11, bottom right). Since the trend in the March PDO index over 1970–2019 is very small,[2] the contribution of the trend in the PDO to the z_{200} trend is also small (less than 30 m over 50 years), and the non-PDO-related z_{200} trend closely resembles the variability associated with low non-PDO-related precipitation in the interior Southwest. While the PDO in this season likely influences precipitation in the interior Southwest in March, there is clear evidence of a trend toward an atmospheric circulation pattern independent of the PDO, which is in turn related to the precipitation decline in the interior Southwest.

What then could be driving the clear stationary wave trend in March? An anomalous stationary wave could arise from a change in the forcing, either thermal or orographical (Held et al. 2002; Wills et al. 2019). Figure 12 shows the trends in meridional winds and vertical velocity in March over the North Pacific averaged over 30°–40°N, along with the trends in surface heat fluxes and sea surface temperature (SST) by longitude. Precipitation across the North Pacific is largely consistent with the circulation patterns: where there is more upward vertical motion and advection of warm moist air from the south, precipitation increases, and vice versa for regions of decreasing precipitation. There is an increase in SSTs west of the date line, which could at first appear to be a source for thermal forcing of the wave. However, the upward latent and sensible heat fluxes decrease in this same region, and the turbulent fluxes tend to increase where the precipitation is reduced. This implies that the surface ocean is in fact responding to

[2] The sign of the March PDO trend differs based on PDO index used. While here we use the PDO index as in Mantua et al. (1997), where the trend is slightly positive, the trend in the National Oceanic and Atmospheric Administration (NOAA) National Centers for Environmental Information (NCEI) PDO index over this period is small but negative. This does not affect our overall conclusion that the PDO contribution to the z_{200} trend is small.

Brought to you by NOAA Central Library | Unauthenticated | Downloaded 08/28/24 07:28 PM UTC

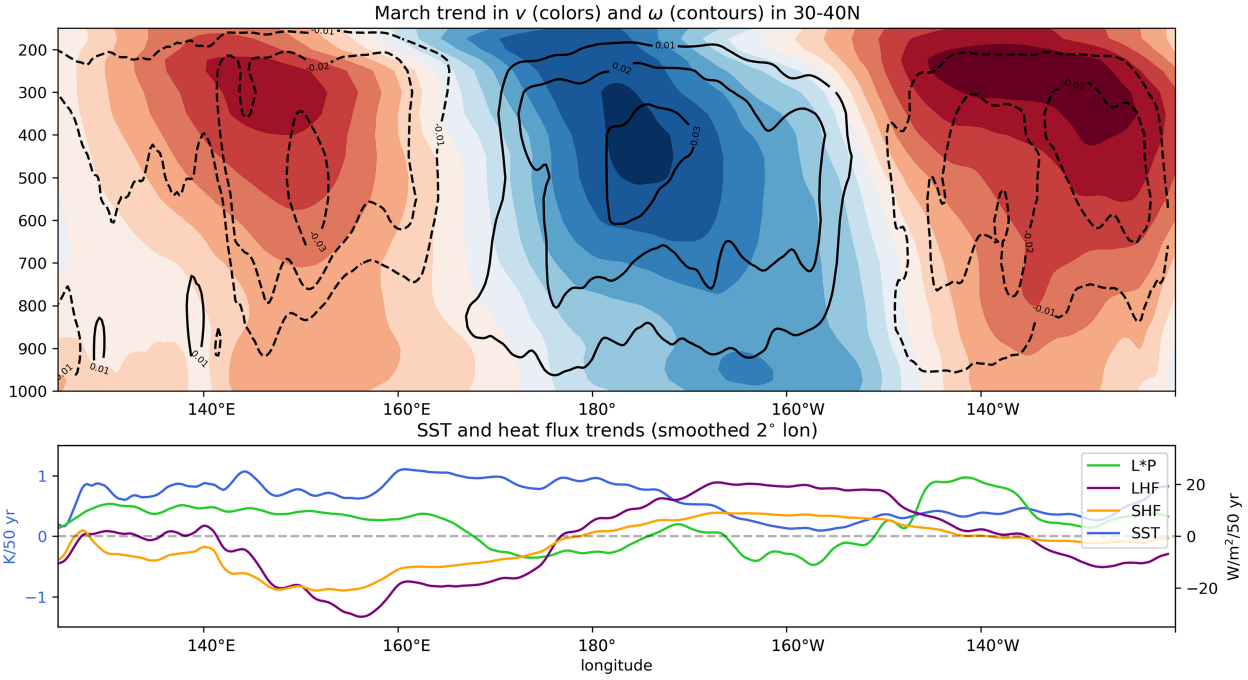


FIG. 12. (top) Contours show trends over 1970–2019 in March meridional winds (v; colors; contour intervals of 0.75 in units of m s^{-1} per 50 years; red indicates northward winds) and subsidence (ω; contours; Pa s^{-1} per 50 years) at pressure levels (mb) over the North Pacific, averaged over 30°–40°N. Subsidence values are smoothed by a 2° rolling mean in longitude. (bottom) Lines show trends in $L \times$ precipitation, where L is the latent heat of vaporization of water (green), SST (blue), latent heat flux (purple), and sensible heat flux (orange), both positive upward and averaged over 30°–40°N and smoothed by a 2° rolling mean in longitude. The SST trend axis is given in blue on the right-hand side in K per 50 years, and the other quantities are in W m^{-2} per 50 years.

the atmosphere, with, for example, southerly flow enhancing moist advection inducing precipitation, suppressing surface turbulent heat fluxes, and warming SSTs. That is, the SSTs appear to be responding to, not forcing, the wave pattern. Thus we speculate that this wave arises from a change in circulation patterns perhaps due to a change in the mean flow field through which a forced wave propagates, or from changes in eddy-mean flow interactions, or diabatic heating elsewhere, rather than from a local change in diabatic heating in the extratropical Pacific or from decadal-scale Pacific SST variability, but understanding the exact forcing mechanism is outside the scope of the current study.

6. Contribution to June burned area increase

We can see qualitatively from the positive relationship between VPD and burned area (Fig. 1) and the definition of VPD as $e_s - e_a$ that declining vapor pressure should tend to increase burned area for a given change in temperature. We can further compare the effects of declining vapor pressure and increasing saturation vapor pressure on June burned forest area in the interior Southwest. Since the adherence of vapor pressure scaling to Clausius–Clapeyron in a warming atmosphere relies on relative humidity remaining approximately fixed, we compare these to burned area predicted in fixed relative humidity scenarios.

First, we calculate the slope (a) of the linear regression[3] between anomalies of the natural logarithm of June burned forest area and anomalies of March–July (MAMJJ) VPD, with anomalies calculated from the 1984–2019 mean (Fig. 13, right). The regression intercept is zero by design. To represent the effect of increasing VPD over the 1984–2019 period on log of June burned forest area [$\widetilde{\ln(\mathrm{BA}_{\mathrm{pred}})}$], we calculate the least squares best fit line through the nondetrended MAMJJ VPD anomaly $\widetilde{\mathrm{VPD}}_{\mathrm{MAMJJ}}$ and multiply this by a:

$$\widetilde{\ln(\mathrm{BA}_{\mathrm{pred}})} = a \times \widetilde{\mathrm{VPD}}_{\mathrm{MAMJJ}}. \quad (4)$$

This uses the relation between VPD and log of burned area to convert the trend in VPD to a trend in log of burned area. The

[3] The strong relationship between burned forest area and VPD in the Southwest ($r = 0.78$ in this region for these seasons) is driven largely by covariability in the high-frequency interannual variations of the two quantities rather than coincidental trends. In the western United States, the relationship between log of burned area and VPD appears to have been stable over recent decades, and a similar approach of modeling burned area using VPD, trained on only twentieth-century data, was well able to predict the increase in burned area in the 2000s (Williams et al. 2019; Abatzoglou et al. 2021; Turco et al. 2023). Thus, we are confident that the strong correlation between VPD and burned area represents a mechanistic link and is not due simply to coinciding trends.

Brought to you by NOAA Central Library | Unauthenticated | Downloaded 08/28/24 07:28 PM UTC

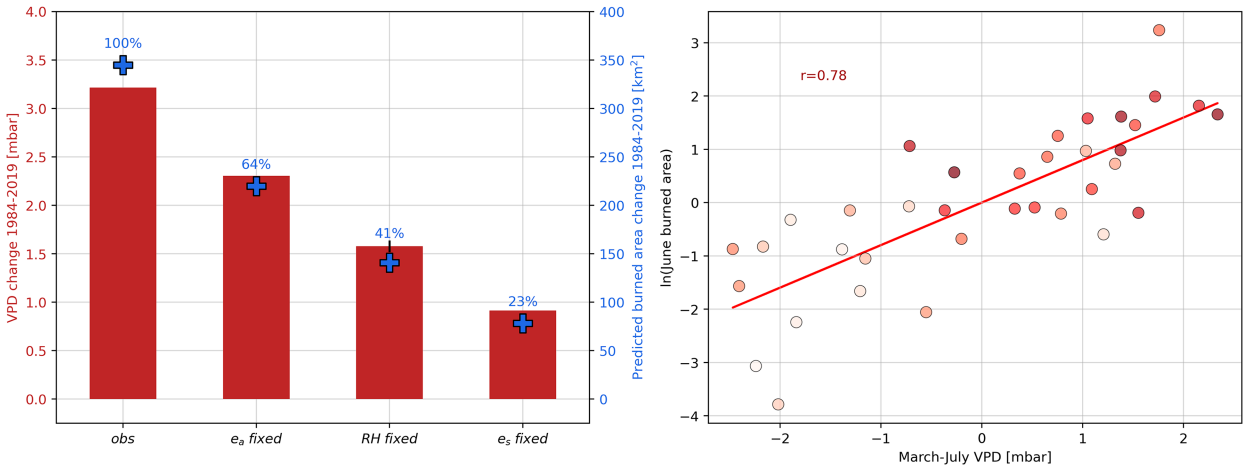


FIG. 13. (left) For various VPD scenarios (observed e_a and e_s, fixed e_a, fixed relative humidity, and fixed e_s), the slopes of the linear increase in MAMJJ VPD in the interior southwest from 1984 to 2019 (red bars; mb), and associated modeled June burned forest area increases (blue crosses; km^2). The error bar on the fixed relative humidity bar represents one standard deviation within the 46 RH scenarios used. Percentages represent the percent of the average value of the burned area increase with respect to the increase modeled using observed VPD. (right) The anomaly of the natural log of June burned area in the interior Southwest vs the MAMJJ VPD anomaly for each year from 1984 to 2019. Scatters are colored by year, with more recent years darker red. The red line represents the linear fit, used to estimate changes in June burned area from changes in MAMJJ VPD.

VPD-predicted log of burned area can then be calculated by adding back the observed mean log of burned area [$\overline{\ln(\mathrm{BA_{pred}})}$]:

$$\ln(\mathrm{BA_{pred}}) = \widetilde{\ln(\mathrm{BA_{pred}})} + \overline{\ln(\mathrm{BA_{obs}})}, \tag{5}$$

which ensures the mean of the predicted burned area equals the mean of observed burned area.

This is also done for a set of alternative MAMJJ VPD anomaly time series ($\mathrm{VPD^*_{MAMJJ}}$) in three scenarios: 1) fixed vapor pressure and actual saturation vapor pressure, 2) fixed relative humidity and actual saturation vapor pressure, and 3) fixed saturation vapor pressure and actual vapor pressure. For the fixed relative humidities, each $\mathrm{RH_{MAMJJ},\mathit{i}}$ we use is one of the 46 possible 5-yr averaged relative humidities from the 1970 to 2019 period. This is done to capture a realistic range of possible fixed relative humidity scenarios. For the fixed e_a and e_s scenarios we use their climatological values in MAMJJ over 1970–2019 (using different values for these will not affect the slope of VPD trends due to their linear relationships to VPD). For each alternative scenario the VPD anomaly is calculated by removing the 1984–2019 mean (for consistency with the VPD values used to calculate their regression slope a). We then use the linear least squares fits to the $\mathrm{VPD^*_{MAMJJ}}$ time series ($\widetilde{\mathrm{VPD^*_{MAMJJ}}}$) and the relationship in Eqs. (4) and (5) to estimate the logarithm of June burned forest area in the alternative scenarios [$\ln(\mathrm{BA^*_{pred}})$]:

$$\ln(\mathrm{BA^*_{pred}}) = a \times \widetilde{\mathrm{VPD^*_{MAMJJ}}} + \overline{\ln(\mathrm{BA_{obs}})}.$$

To calculate the change in observed burned area we use an exponential fit to the observed burned area time series and take the difference between the 2019 and 1984 values of the exponential model, giving an increase of 528 km^2. To calculate changes in burned area predicted by VPD and the three different VPD* scenarios, we exponentiate $\ln(\mathrm{BA_{pred}})$ and $\ln(\mathrm{BA^*_{pred}})$ as in Eqs. (4) and (5) to get the difference between the 2019 and 1984 values.

The estimate of the VPD-induced change in observed June burned forest area (leftmost blue cross in Fig. 13) accounts for about two-thirds of the observed change in burned area (345 km^2 compared to the observed change of 528 km^2) indicating that non-VPD factors, such as other climate variables, land-use and land-cover change, and other influences, have contributed to the increase in burned area. The linear increase in VPD over 1984–2019 was 3.21 mb (leftmost red bar in Fig. 13). In the fixed relative humidity case, we average the 46 values of the linear increases in VPD to get the mean and show this together with the standard deviation in Fig. 13. In the fixed relative-humidity scenario, VPD increased by 1.58 mb. Notably, the contribution to the linear increase in VPD from the humidity change relative to fixed relative humidity (1.63 mb) is therefore larger than the contribution that would arise from rising saturation humidity under fixed relative humidity assumptions (1.58 mb). In the fixed vapor pressure case, VPD increases by 2.30 mb, and in the case where no warming (i.e., saturation vapor pressure increase) occurs, VPD still increases by 0.9 mb.

We find that the change in burned area in the alternative scenarios reproduce 64% (fixed e_a), 41% ± 2% (average fixed RH), and 23% (fixed e_s) of the VPD-induced burned area increase.[4] Even in the counterfactual scenario where no increase in temperature occurs, burned area increases due to

[4] Note that the fixed e_a and fixed e_s percentages do not add up to 100% due to the nonlinearity of the modeled burned area. Thus, we are not separating the observed VPD-induced burned area increase into its temperature and humidity components, rather we model these alternative scenarios for a baseline of possible burned area change in different cases.

Brought to you by NOAA Central Library | Unauthenticated | Downloaded 08/28/24 07:28 PM UTC

the decline in humidity. Thus the decline in vapor pressure has likely contributed significantly to the magnitude of the burned forest area increase in the interior over 1984–2019.

7. Conclusions and discussion

Here, we have identified various fire-favorable antecedent climate drivers of summer forest fire in the interior and coastal southwestern United States. We then examined a decline in lower-tropospheric vapor pressure for specific months in both the coastal and interior Southwest from 1970 to 2019. Turning our focus to the interior drying in the months bridging spring into summer, we explained the contributions to such a humidity decline, parsing out the various roles of surface processes, atmospheric dynamics, and seasonality. We traced the mechanism behind this regionally and seasonally specific lower-tropospheric drying to a trend in the large-scale circulation in early spring that affects the surface water balance in later months via a precipitation deficit. Our main conclusions are as follows:

- There is good agreement between reanalysis and station data that vapor pressure e_a has decreased in various parts of the western United States in every season from 1970 to 2019. There is even better agreement that one primary region and time where this drying is occurring is in the interior Southwest during the months of March–June. Regions and seasons where vapor pressure is decreasing see an amplified increase in VPD compared to the warming-driven increase alone.
- Climatologically, the interior Southwest receives maximum precipitation in July from the North American monsoon, but also receives precipitation in winter months from the storm track. This drives an evaporation seasonality that peaks in the summer during the monsoon. During the monsoon months (July, August, and September), the mean flow converges moisture into the column mostly though orographic lift and mass convergence, while transient eddies diverge moisture. During the rest of the year, transient eddies converge moisture into the column and the mean flow diverges moisture away through advection and subsidence.
- The lower-tropospheric drying trend in this region is driven by a perturbation of this water balance. A long-term reduction in precipitation, primarily in March, decreases the amount of water in the soil that is available to evaporate into the lower atmosphere in the following months. This decreased evaporation is the most likely cause of the observed lower-tropospheric drying. In response to the reduced evaporative flux into the atmosphere, the circulation converges more moisture via the mean flow and transient eddy moisture convergences.
- The negative trend in March precipitation over the interior Southwest from 1970 to 2019 is a robust feature of precipitation observations. The March precipitation trend is associated with a significant trend toward an extratropical wavenumber-4 stationary wave that places a high pressure trend over the western United States and drying easterlies over the interior Southwest region. This wave is likely not forced by diabatic heating over the extratropical Pacific or decadal-scale Pacific SST variability but rather some other change in circulation.
- Using the observed exponential relationship between VPD and burned forest area, we estimate that with no change in vapor pressure, the temperature increase alone would lead to an increase in VPD-induced burned area equal to 64% of the observed VPD-induced burned area increase over 1984–2019. In fixed relative humidity scenarios, the associated burned area increase would equal 41% of the observed VPD-induced burned area increase. In a scenario with no change in temperature at all but with the observed decline in vapor pressure, the humidity decline alone would lead to a burned area increase equal to 23% of the observed VPD-induced increase in burned area.

While we have traced the mechanism behind the drying trend in the interior Southwest to a change in the large-scale atmospheric circulation in early spring, several matters remain to be investigated regarding these decadal-scale changes. It needs to be determined what the relative roles of natural climate variability and anthropogenic forcing are in causing the circulation changes that reduce late winter/early spring precipitation in the region. Here, we have described in detail the circulation patterns, precipitation and soil moisture trends that have contributed to the observed humidity decline within the interior Southwest. From the results of Simpson et al. (2023), which suggests that arid and semiarid regions of the world are not showing a rise in specific humidity on average, it appears that there may be two factors at play that have allowed the Southwest to exhibit such a substantial vapor pressure decline. As we have outlined here, the region has experienced a precipitation decline. This, combined with the assessment in Simpson et al. (2023) that a Clausius–Clapeyron rise in specific humidity over arid and semiarid regions is not occurring, has allowed the Southwest to experience a substantial vapor pressure decline under this precipitation trend, despite the rising temperatures.

In the bulk of this study, we have only examined the causes of this drying trend in the *interior* Southwest during the months leading into summertime. However, a negative vapor pressure trend is observed in other parts of the western United States during other seasons, for example, the coastal drying in California that intensifies in autumn. Simpson et al. (2023) show that over the 1980–2020 period in the Southwest, the e_a decline is relatively consistent year-round when expressed as a percentage of the climatological e_a. In all of the regions in the western United States with decreasing rather than increasing vapor pressure, the observed decadal time scale drying likely has encouraged forest fire activity. Record-breaking wildfire seasons in the West, usually associated with anomalously high VPD driven by high temperatures, have been found to coincide with anomalously high VPD driven by low atmospheric moisture (Williams et al. 2014a). It is also becoming increasingly clear that, due to the exponential response of burned forest area to VPD, record-breaking wildfire seasons do not necessarily require record-breaking anomalies in VPD, temperature, or atmospheric moisture (Juang et al. 2022). Therefore, it is essential from a fire-risk standpoint to 1) identify forest-fire-prone regions in the West where vapor pressure is decreasing (rather than increasing as

Brought to you by NOAA Central Library | Unauthenticated | Downloaded 08/28/24 07:28 PM UTC

expected by Clausius–Clapeyron) and thus contributing to the warming-driven increase in VPD; 2) understand the mechanisms in the land surface, atmosphere, and perhaps ocean, behind the near-surface atmospheric drying; and, more broadly, 3) understand why the average change in specific humidity over arid and semiarid regions is near zero despite the warming atmosphere.

Acknowledgments. T. W. P. J. was supported by the National Science Foundation Graduate Research Fellowship Program. R. S. and H. L. were supported by the National Oceanic and Atmospheric Administration Awards NA20OAR4310379 and NA20OAR4310425 and National Science Foundation Award AGS-2127684. A. P. W. was supported by the Zegar Family Foundation and the Moore Foundation. I. R. S. was supported by NCAR, which is a major facility sponsored by the National Science Foundation under Cooperative Agreement 1852977 and NOAA MAPP Award NA200AR4310413. K. A. M. was supported by National Science Foundation Award AGS-1939988.

Data availability statement. The ERA5 data used in this study are freely available from the ECMWF website (https://www.ecmwf.int/en/forecasts/datasets/reanalysis-datasets/era5). The precipitation products used are available from PRISM (https://prism.oregonstate.edu/), CRU (https://crudata.uea.ac.uk/cru/data/hrg/), and MSWEP (https://www.gloh2o.org/mswep/). NLDAS-2 Noah soil moisture can be accessed at https://disc.gsfc.nasa.gov/ and GLEAM soil moisture at https://www.gleam.eu/. The Integrated Surface Database station data is available at https://www.ncei.noaa.gov/products/land-based-station/integrated-surface-database. The MTBS burned area and NLCD forest cover datasets are available at https://www.mtbs.gov/ and https://www.mrlc.gov/data, respectively. The PDO index used is available at http://research.jisao.washington.edu/data_sets/pdo/.

REFERENCES

Abatzoglou, J. T., and A. P. Williams, 2016: Impact of anthropogenic climate change on wildfire across western US forests. *Proc. Natl. Acad. Sci. USA*, **113**, 11 770–11 775, https://doi.org/10.1073/pnas.1607171113.

——, D. S. Battisti, A. P. Williams, W. D. Hansen, B. J. Harvey, and C. A. Kolden, 2021: Projected increases in western US forest fire despite growing fuel constraints. *Commun. Earth Environ.*, **2**, 227, https://doi.org/10.1038/s43247-021-00299-0.

Adams, D. K., and A. C. Comrie, 1997: The North American monsoon. *Bull. Amer. Meteor. Soc.*, **78**, 2197–2214, https://doi.org/10.1175/1520-0477(1997)078<2197:TNAM>2.0.CO;2.

Awange, J. L., K. X. Hu, and M. Khaki, 2019: The newly merged satellite remotely sensed, gauge and reanalysis-based multi-source weighted-ensemble precipitation: Evaluation over Australia and Africa (1981–2016). *Sci. Total Environ.*, **670**, 448–465, https://doi.org/10.1016/j.scitotenv.2019.03.148.

Boos, W. R., and S. Pascale, 2021: Mechanical forcing of the North American monsoon by orography. *Nature*, **599**, 611–615, https://doi.org/10.1038/s41586-021-03978-2.

Brown, P. J., and A. T. DeGaetano, 2013: Trends in U.S. surface humidity, 1930–2010. *J. Appl. Meteor. Climatol.*, **52**, 147–163, https://doi.org/10.1175/JAMC-D-12-035.1.

Byrne, M. P., and P. A. O'Gorman, 2015: The response of precipitation minus evapotranspiration to climate warming: Why the "wet-get-wetter, dry-get-drier" scaling does not hold over land. *J. Climate*, **28**, 8078–8092, https://doi.org/10.1175/JCLI-D-15-0369.1.

Chiodi, A. M., B. E. Potter, and N. K. Larkin, 2021: Multi-decadal change in western US nighttime vapor pressure deficit. *Geophys. Res. Lett.*, **48**, e2021GL092830, https://doi.org/10.1029/2021GL092830.

Cook, B. I., J. E. Smerdon, R. Seager, and S. Coats, 2014: Global warming and 21st century drying. *Climate Dyn.*, **43**, 2607–2627, https://doi.org/10.1007/s00382-014-2075-y.

Dai, A., 2006: Recent climatology, variability, and trends in global surface humidity. *J. Climate*, **19**, 3589–3606, https://doi.org/10.1175/JCLI3816.1.

Daly, C., M. Halbleib, J. I. Smith, W. P. Gibson, M. K. Doggett, G. H. Taylor, J. Curtis, and P. P. Pasteris, 2008: Physiographically sensitive mapping of climatological temperature and precipitation across the conterminous United States. *Int. J. Climatol.*, **28**, 2031–2064, https://doi.org/10.1002/joc.1688.

Douglas, M. W., R. A. Maddox, K. Howard, and S. Reyes, 1993: The Mexican monsoon. *J. Climate*, **6**, 1665–1677, https://doi.org/10.1175/1520-0442(1993)006<1665:TMM>2.0.CO;2.

Douville, H., S. Qasmi, A. Ribes, and O. Bock, 2022: Global warming at near-constant tropospheric relative humidity is supported by observations. *Commun. Earth Environ.*, **3**, 237, https://doi.org/10.1038/s43247-022-00561-z.

Finco, M., B. Quayle, Y. Zhang, J. Lecker, K. A. Megown, and C. K. Brewer, 2012: Monitoring Trends and Burn Severity (MTBS): Monitoring wildfire activity for the past quarter century using Landsat data. *Moving from Status to Trends: Forest Inventory and Analysis (FIA) Symp. 2012*, Newtown Square, PA, U.S. Department of Agriculture, Forest Service, Northern Research Station, 222–228, https://www.nrs.fs.usda.gov/pubs/gtr/gtr-nrs-p-105papers/35finco-p-105.pdf.

Gelaro, R., and Coauthors, 2017: The Modern-Era Retrospective Analysis for Research and Applications, version 2 (MERRA-2). *J. Climate*, **30**, 5419–5454, https://doi.org/10.1175/JCLI-D-16-0758.1.

Gimeno, L., and Coauthors, 2020: Recent progress on the sources of continental precipitation as revealed by moisture transport analysis. *Earth-Sci. Rev.*, **201**, 103070, https://doi.org/10.1016/j.earscirev.2019.103070.

Harris, I., T. J. Osborn, P. Jones, and D. Lister, 2020: Version 4 of the CRU TS monthly high-resolution gridded multivariate climate dataset. *Sci. Data*, **7**, 109, https://doi.org/10.1038/s41597-020-0453-3.

Held, I. M., and B. J. Soden, 2006: Robust responses of the hydrological cycle to global warming. *J. Climate*, **19**, 5686–5699, https://doi.org/10.1175/JCLI3990.1.

——, M. Ting, and H. Wang, 2002: Northern winter stationary waves: Theory and modeling. *J. Climate*, **15**, 2125–2144, https://doi.org/10.1175/1520-0442(2002)015<2125:NWSWTA>2.0.CO;2.

Hersbach, H., and Coauthors, 2020: The ERA5 global reanalysis. *Quart. J. Roy. Meteor. Soc.*, **146**, 1999–2049, https://doi.org/10.1002/qj.3803.

Homer, C. H., J. A. Fry, and C. A. Barnes, 2012: The National Land Cover Database. U.S. Geological Survey Fact Sheet, 4 pp., https://pubs.usgs.gov/fs/2012/3020/fs2012-3020.pdf.

Brought to you by NOAA Central Library | Unauthenticated | Downloaded 08/28/24 07:28 PM UTC

Jacobson, T. W. P., R. Seager, A. P. Williams, and N. Henderson, 2022: Climate dynamics preceding summer forest fires in California and the extreme case of 2018. *J. Appl. Meteor. Climatol.*, **61**, 989–1002, https://doi.org/10.1175/JAMC-D-21-0198.1.

Juang, C. S., A. P. Williams, J. T. Abatzoglou, J. K. Balch, M. D. Hurteau, and M. A. Moritz, 2022: Rapid growth of large forest fires drives the exponential response of annual forest-fire area to aridity in the western United States. *Geophys. Res. Lett.*, **49**, e2021GL097131, https://doi.org/10.1029/2021GL097131.

Kobayashi, S., and Coauthors, 2015: The JRA-55 reanalysis: General specifications and basic characteristics. *J. Meteor. Soc. Japan*, **93**, 5–48, https://doi.org/10.2151/jmsj.2015-001.

Lehner, F., C. Deser, I. R. Simpson, and L. Terray, 2018: Attributing the U.S Southwest's recent shift into drier conditions. *Geophys. Res. Lett.*, **45**, 6251–6261, https://doi.org/10.1029/2018GL078312.

Mankin, J. S., R. Seager, J. E. Smerdon, B. I. Cook, and A. P. Williams, 2019: Mid-latitude freshwater availability reduced by projected vegetation responses to climate change. *Nat. Geosci.*, **12**, 983–988, https://doi.org/10.1038/s41561-019-0480-x.

Mantua, N. J., S. R. Hare, Y. Zhang, J. M. Wallace, and R. C. Francis, 1997: A Pacific interdecadal climate oscillation with impacts on salmon production. *Bull. Amer. Meteor. Soc.*, **78**, 1069–1080, https://doi.org/10.1175/1520-0477(1997)078<1069:APICOW>2.0.CO;2.

Martens, B., and Coauthors, 2017: GLEAM v3: Satellite-based land evaporation and root-zone soil moisture. *Geosci. Model Dev.*, **10**, 1903–1925, https://doi.org/10.5194/gmd-10-1903-2017.

McKinnon, K. A., A. Poppick, and I. R. Simpson, 2021: Hot extremes have become drier in the United States southwest. *Nat. Climate Change*, **11**, 598–604, https://doi.org/10.1038/s41558-021-01076-9.

O'Gorman, P. A., and C. J. Muller, 2010: How closely do changes in surface and column water vapor follow Clausius–Clapeyron scaling in climate change simulations? *Environ. Res. Lett.*, **5**, 025207, https://doi.org/10.1088/1748-9326/5/2/025207.

Scheff, J., and J. C. Burroughs, 2023: Diverging trends in US summer dewpoint since 1948. *Int. J. Climatol.*, **43**, 4183–4195, https://doi.org/10.1002/joc.8081.

Seager, R., and N. Henderson, 2013: Diagnostic computation of moisture budgets in the ERA-interim reanalysis with reference to analysis of CMIP-archived atmospheric model data. *J. Climate*, **26**, 7876–7901, https://doi.org/10.1175/JCLI-D-13-00018.1.

——, and M. Hoerling, 2014: Atmosphere and ocean origins of North American droughts. *J. Climate*, **27**, 4581–4606, https://doi.org/10.1175/JCLI-D-13-00329.1.

——, and Coauthors, 2014: Dynamical and thermodynamical causes of large-scale changes in the hydrological cycle over North America in response to global warming. *J. Climate*, **27**, 7921–7948, https://doi.org/10.1175/JCLI-D-14-00153.1.

——, A. Hooks, A. P. Williams, B. Cook, J. Nakamura, and N. Henderson, 2015: Climatology, variability, and trends in the U.S. vapor pressure deficit, an important fire-related meteorological quantity. *J. Appl. Meteor. Climatol.*, **54**, 1121–1141, https://doi.org/10.1175/JAMC-D-14-0321.1.

——, T. J. Osborn, Y. Kushnir, I. R. Simpson, J. Nakamura, and H. Liu, 2019: Climate variability and change of Mediterranean-type climates. *J. Climate*, **32**, 2887–2915, https://doi.org/10.1175/JCLI-D-18-0472.1.

——, M. Ting, P. Alexander, J. Nakamura, H. Liu, C. Li, and I. R. Simpson, 2022: Mechanisms of a meteorological drought onset: Summer 2020 to spring 2021 in southwestern North America. *J. Climate*, **35**, 7367–7385, https://doi.org/10.1175/JCLI-D-22-0314.1.

Simpson, I. R., K. A. McKinnon, D. Kennedy, D. M. Lawrence, F. Lehner, and R. Seager, 2023: Observed humidity trends in dry regions contradict climate models. *Proc. Natl. Acad. Sci. USA*, **121**, e2302480120, https://doi.org/10.1073/pnas.2302480120.

Smith, A., N. Lott, and R. Vose, 2011: The Integrated Surface Database: Recent developments and partnerships. *Bull. Amer. Meteor. Soc.*, **92**, 704–708, https://doi.org/10.1175/2011BAMS3015.1.

Swann, A. L. S., F. M. Hoffman, C. D. Koven, and J. T. Randerson, 2016: Plant responses to increasing CO_2 reduce estimates of climate impacts on drought severity. *Proc. Natl. Acad. Sci. USA*, **113**, 10 019–10 024, https://doi.org/10.1073/pnas.1604581113.

Ting, M., R. Seager, C. Li, H. Liu, and N. Henderson, 2018: Mechanism of future spring drying in the southwestern United States in CMIP5 models. *J. Climate*, **31**, 4265–4279, https://doi.org/10.1175/JCLI-D-17-0574.1.

Turco, M., J. T. Abatzoglou, S. Herrera, Y. Zhuang, S. Jerez, D. D. Lucas, A. AghaKouchak, and I. Cvijanovic, 2023: Anthropogenic climate change impacts exacerbate summer forest fires in California. *Proc. Natl. Acad. Sci. USA*, **120**, e2213815120, https://doi.org/10.1073/pnas.2213815120.

Westerling, A. L., H. G. Hidalgo, D. R. Cayan, and T. W. Swetnam, 2006: Warming and earlier spring increase western U.S. forest wildfire activity. *Science*, **313**, 940–943, https://doi.org/10.1126/science.1128834.

Williams, A. P., and Coauthors, 2014a: Causes and implications of extreme atmospheric moisture demand during the record-breaking 2011 wildfire season in the southwestern United States. *J. Appl. Meteor. Climatol.*, **53**, 2671–2684, https://doi.org/10.1175/JAMC-D-14-0053.1.

——, and Coauthors, 2014b: Correlations between components of the water balance and burned area reveal new insights for predicting forest fire area in the southwest United States. *Int. J. Wildland Fire*, **24**, 14–26, https://doi.org/10.1071/WF14023.

——, J. T. Abatzoglou, A. Gershunov, J. Guzman-Morales, D. A. Bishop, J. K. Balch, and D. P. Lettenmaier, 2019: Observed impacts of anthropogenic climate change on wildfire in California. *Earth's Future*, **7**, 892–910, https://doi.org/10.1029/2019EF001210.

——, and Coauthors, 2020: Large contribution from anthropogenic warming to an emerging North American megadrought. *Science*, **368**, 314–318, https://doi.org/10.1126/science.aaz9600.

——, B. I. Cook, and J. E. Smerdon, 2022: Rapid intensification of the emerging southwestern North American megadrought in 2020–2021. *Nat. Climate Change*, **12**, 232–234, https://doi.org/10.1038/s41558-022-01290-z.

Wills, R. C. J., R. H. White, and X. J. Levine, 2019: Northern Hemisphere stationary waves in a changing climate. *Curr. Climate Change Rep.*, **5**, 372–389, https://doi.org/10.1007/s40641-019-00147-6.

Xia, Y., and Coauthors, 2012: Continental-scale water and energy flux analysis and validation for the North American Land Data Assimilation System project phase 2 (NLDAS-2): 1. Intercomparison and application of model products. *J. Geophys. Res.*, **117**, D03109, https://doi.org/10.1029/2011JD016048.

Zhuang, Y., R. Fu, B. D. Santer, R. E. Dickinson, and A. Hall, 2021: Quantifying contributions of natural variability and anthropogenic forcings on increased fire weather risk over the western United States. *Proc. Natl. Acad. Sci. USA*, **118**, e2111875118, https://doi.org/10.1073/pnas.2111875118.

Brought to you by NOAA Central Library | Unauthenticated | Downloaded 08/28/24 07:28 PM UTC